Journal of Rock Mechanics and Geotechnical Engineering xxx (xxxx) xxx

Contents lists available at ScienceDirect

Journal of Rock Mechanics and Geotechnical Engineering

journal homepage: www.jrmge.cn

Full Length Article

Structural behavior of triple-layer composite lining of a water conveyance tunnel: Insight from full-scale loading tests

De-Yang Wang [a], Hong-Hu Zhu [a, *], Xue-Hui Zhang [b], Jing-Wu Huang [c], Zhen-Rui Yan [c], Dao-Yuan Tan [a], Shao-Qun Lin [b]

[a] School of Earth Sciences and Engineering, Nanjing University, Nanjing, 210023, China
[b] Department of Civil and Environmental Engineering, The Hong Kong Polytechnic University, Hung Hom, Kowloon, Hong Kong, China
[c] Guangdong Hydropower Planning & Design Institute, Guangzhou, 510635, China

ARTICLE INFO

Article history:
Received 4 September 2024
Received in revised form
27 October 2024
Accepted 24 November 2024
Available online xxx

Keywords:
Composite lining
Full-scale test
Interface
Fiber optic sensor
Mechanical behavior

ABSTRACT

When constructing water conveyance shield tunnels under high internal pressure, composite linings are preferred over single-layer segmental linings due to the superior water tightness and load-bearing capacity. A triple-layer composite lining, consisting of an outer segmental lining, internal steel tube, and self-compacting concrete (SCC) filling, has recently been applied in a large-scale water conveyance tunnel project in China. However, its structural behavior under external overburden and internal water pressures remains poorly understood. This study investigates the mechanical behavior of the triple-layer composite lining through full-scale loading tests using a novel platform that simulates external and internal pressures. Results show that the composite lining remains highly elastic under combined loads with an internal pressure of 0.4 MPa. When the internal pressure increases to 0.6 MPa, cracks first appear in the SCC layer near segment joints, propagating uniformly and leading to stress redistribution. Studs on the steel tube-SCC interface strengthen bonding, reducing debonding at this interface while slightly increasing debonding at the SCC-segment interface. Despite localized SCC damage, the lining maintains excellent serviceability under cyclic pressure fluctuations. This study offers valuable insights for the design and construction of water conveyance shield tunnels with triple-layer composite linings, particularly in high-pressure environments.

1. Introduction

The shield tunneling method has been extensively used for constructing various types of tunnels, including traffic tunnels, service tunnels, and water conveyance tunnels, due to higher construction efficiency and safety assurance compared with the conventional mining method (Armaghani et al., 2019; Huang et al., 2022). For roadway or railway traffic tunnels, external overburden pressure dominates and determines the tunnel lining deformation, which tends to trigger compression status within the cross-section, therefore a single-layer segmental lining (in Fig. 1a) is mostly sufficient to bear the loading. However, for water conveyance tunnels, the internal water pressure, which may reach as high as 1.2 MPa (Liu et al., 2021), plays a vital role in the deformation behavior and tends to trigger significant tension within the tunnel lining, which could deteriorate the structure integrity and water tightness. Thus, composite lining, rather than the single-layer segmental lining, is preferred in water conveyance tunnels for its higher water tightness and bearing capacity, which has been shown in the representative water conveyance tunnel projects as summarized in Table 1.

The composite lining in water conveyance tunnels is typically constructed by concreting a secondary lining inside or even an additional steel lining to improve its water tightness and long-term serviceability (see Fig. 1b and c). Due to the high internal water pressures and external overburden pressure, these composite lining structures undergo complex deformations (Zhou et al., 2022; Wang et al., 2023), especially for the triple-layer composite lining. However, there are currently few studies on its mechanical behavior under complex loading conditions that combine external ground loads and internal water pressure.

Extensive research has been conducted on the mechanical behavior of tunnel linings through various methods, including numerical simulation (Van Oorsouw, 2010; Jin et al., 2017; Chen

* Corresponding author.
E-mail address: zhh@nju.edu.cn (H.-H. Zhu).

https://doi.org/10.1016/j.jrmge.2024.11.025

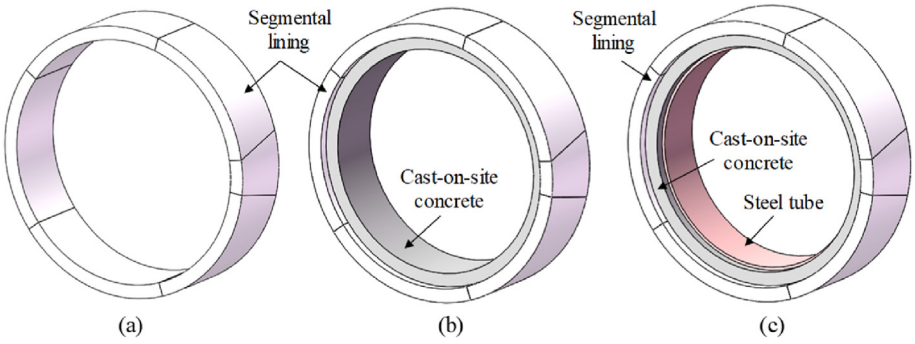

Fig. 1. Schematics of (a) single-layer, (b) double-layer and (c) triple-layer composite linings of the water conveyance tunnel.

Table 1
Summary of typical case studies of water conveyance tunnels.

Project	Location	Total length (km)	Tunnel outer diameter (m)	Internal pressure (MPa)	Structural type	Source
Guangzhou Xijiang water diversion project	Guangzhou, China	47.6	3.6	0.6	Double-layer lining	Yang et al. (2013)
Qingcaosha water conveyance tunnel	Shanghai, China	7.23	6.4	0.45	Single-layer lining	Chen et al. (2014)
Yellow River crossing tunnel	Henan, China	3.45	8.7	0.51	Double-layer lining	Yang et al. (2018)
Kerman water conveyance tunnel	Kerman, Iran	38	4.5	–	Double-layer lining	Ahad and Kaveh (2018)
Lanzhou water source construction engineering	Lanzhou, China	31.57	4.6	–	Double-layer lining	Yang et al. (2019)
Qinling water conveyance tunnel	Shaanxi, China	98.3	8.02	1.2	Double-layer lining	Liu et al. (2021)
Deep drainage tunnel of Suzhou River	Shanghai, China	15.3	9	0.6	Double-layer lining	Zhou et al. (2022)

et al., 2020; Zhang et al., 2022), field monitoring (Shi et al., 2003; Mohamad et al., 2010; Zhang et al., 2019; Zhu et al., 2022), scaled loading tests (Guo et al., 2019; Wang et al., 2019), and full-scale loading tests (Zhang et al., 2019; He et al., 2022; Zhou et al., 2022; Bu et al., 2023). Of these, full-scale testing has been particularly instrumental in understanding the real mechanical behavior of tunnel linings, offering insights into structural performance under complex conditions. Early studies established the value of full-scale testing by examining strain and stress distribution in prototype linings. For example, Kashima et al. (1996) conducted prototype tests on rectangular segmental rings to understand strain development in reinforcement and steel members, while Blom (2002) investigated structural behavior and damage patterns in single-layer segmental linings under external loads. Further in situ tests under hard ground conditions by Molins and Arnau (2011) highlighted the critical role of ground-structure interaction on tunnel lining response. Subsequent studies have refined our understanding of lining performance across different structural configurations. Feng et al. (2013) compared the mechanical performance of single-layer and double-layer linings in underwater shield tunnels, showing key differences in load-bearing capacity. In examining composite linings, Yang et al. (2018) demonstrated that membrane-based linings offer simplified and effective load-bearing with enhanced anti-seepage properties for water conveyance tunnels. Zhang et al. (2019) assessed single-layer segmental linings for railway tunnels, introducing effective stiffness and residual bearing capacity coefficients as indicators of structural damage at various failure stages. Bu et al. (2023) investigated failure modes of double-layer composite linings under internal water pressure, offering valuable data for designing resilient tunnel structures in complex environments. Notably, these model test studies predominantly concentrate on deformation mechanism of the single-layer lining or double-layer composite linings under the internal water pressure or external ground loads, while the mechanical behavior of triple-layer composite linings under the combined external ground loads and internal water pressure is rarely reported using full-scale loading tests.

While prior studies have provided valuable insights, significant limitations remain. These include an overemphasis on single- or double-layer linings, limited investigation of combined loading scenarios, and inadequate implementation of advanced monitoring techniques. Addressing these gaps is crucial for a comprehensive understanding of tunnel lining performance under field conditions. This study investigates the mechanical behavior of a special triple-layer composite lining structure, which generally consists of the outermost segmental lining and internal steel tube plus interval concrete filling, by full-scale loading tests. It is worth mentioning that in this test an upgraded loading platform is developed which combines hydraulic jacks and a unique airbags system. Using this platform, both external ground loadings and internal distributed water pressure can be simultaneously imposed, facilitating a more precise simulation of the actual combined loading conditions of the composite lining compared with the previous studies. Furthermore, fiber optic sensing technology is adopted for distributed deformation sensing in the composite lining. The findings from this study contribute to gaining understanding of the structural response and failure mode of composite linings in water-conveyance tunnels.

2. Project overviews

The Pearl River Delta water conveyance tunnel project stands as a significant water conservation endeavor within the Guangdong-

Hong Kong-Macao Greater Bay Area, China. This project is part of the broader initiative to enhance water resource security, distribution, and management across the Greater Bay Area, ensuring a sustainable water supply for the rapidly growing urban areas and industries. As depicted in Fig. 2, the tunnel has a total length of 113.2 km and extends through the core urban agglomeration of the Greater Bay Area. Originating from Liyuzhou in Shunde, Foshan, on the mainstream of the Xijiang River in the west, it culminates at the Gongming Reservoir in Shenzhen to the east. The project construction commenced in 2019 and was completed in August 2023, with a total expenditure of approximately 5.56 billion US dollars. Upon its anticipated inauguration by the end of 2023, the tunnel will play a crucial role in streamlining water resource allocation, alleviating potential water shortages, and supporting the sustainable development of the Greater Bay Area.

The region's advanced economic landscape is characterized by a dense array of underground infrastructures, including deep foundations, metro and highway tunnels, pedestrian pathways, utility tunnels, as well as underground pipelines and parking facilities. The presence of these sensitive infrastructures and urban lifeline projects necessitated the adoption of deep burial strategies for the water conveyance tunnels. As depicted in Fig. 2a, the tunnel section longitudinally has a depth of 40–60 m below the ground surface. The complexity of the surrounding urban environment, combined with the varied geological conditions and the large scale of the project, significantly increased the difficulty of construction. Challenges included maintaining the stability of surrounding structures and minimizing disruptions to existing infrastructures. To ensure construction safety and quality, the shield tunneling method was predominantly employed (Wang et al., 2023) to construct this long tunnel project. Fig. 2b illustrates the tunnel profile from the westernmost water intake station to the easternmost terminal Gongming Reservoir. This alignment comprises 40.9 km dual-tube bored tunnels and 60 km single-tube tunnels, which include approximately 45 km of Tunnel Boring Machine (TBM) tunnels and 15 km of New Austrian Tunneling Method (NATM) tunnels. Notably, a special triple-layer composite lining is widely used to construct about 44.9 km of the water conveyance tunnel as marked with red lines in Fig. 2b.

As illustrated in Fig. 3, the triple-layer composite lining structure consists of an initial concrete segmental ring (at the outermost), an internal steel tube, and the self-compaction concrete (SCC) layer filled between. The initial segmental ring is divided into six segments connected with steel bolts, and each with an average thickness of 300 mm. The standard segments (B1-B1-B3 and L1-L2) possess angles of 72° and 64.5°, respectively, while the key segment (F) has an arc of 15°. The segment concrete is of strength grade C55, and its circumferential reinforcement comprises HRB400 steel rebars. Within a tunnel ring, two M24-type stainless steel bolts are fitted at each radius joint, and ten M24 stainless steel bolts are fitted in the circumferential joint of a full ring. In the composite lining construction, the inner steel tube is first placed and the voids between the tube and outer segmental lining are further filled with SCC. The steel tube features a wall thickness of 14 mm (in this study) and is partially furnished with studs arranged in rows and columns with unequal spacing (400 mm × 350 mm) on the extrados surface (see Fig. 3b), to enhance the steel-concrete

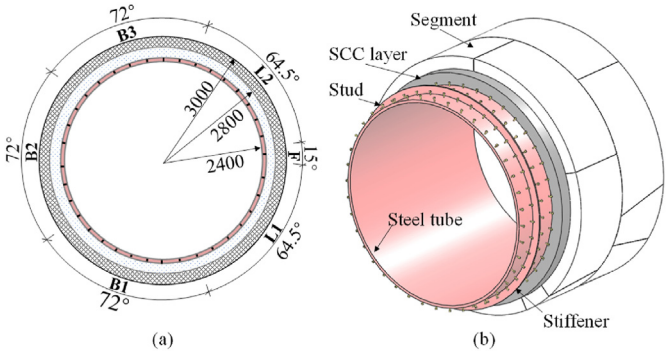

Fig. 3. Illustrations of the studied triple-layer composite lining: (a) cross-section dimensions, and (b) perspective views.

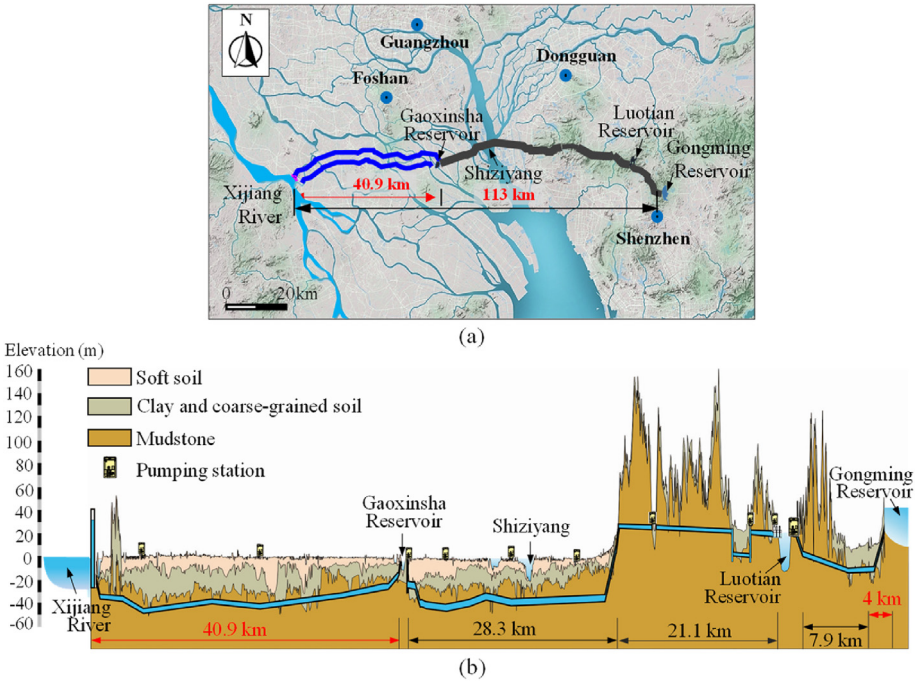

Fig. 2. Schematics of the Pearl River Delta water conveyance project: (a) overall planar view, and (b) stratigraphic profile of the project.

interface bonding. In addition, circumferential stiffeners are welded to the outer steel tube surface at regular intervals of 2000 mm to increase the stiffness of the steel tube and mitigate the undesired deformation in the construction process.

3. Full-scale test arrangement

3.1. Full-scale tests configuration

The full-scale loading tests are conducted using the multifunctional tunnel structure testing system developed by the China Construction Technology Center, as shown in Fig. 4. This platform can perform mechanical performance tests on shield tunnel structural systems with a maximum diameter of 15.6 m and a height of 6 m. To simulate the surrounding ground loading and self-weight acting on the tunnel lining, a total of 24 hydraulic jacks are configured uniformly spaced around the outer circumference of the lining structure. At each loading point, two hydraulic jacks are positioned at different heights, and each jack has the capacity to exert a maximum concentrated force of 2000 kN, as illustrated in Fig. 4b. To prevents local crushing caused by hydraulic jacks, a polyurethane rubber sheet is laid between the distribution beam and the load-bearing surface of the segmental lining's outer wall, serving as a transition layer for force transmission between the steel surface of the distribution beam and the curved concrete surface of the segmental lining. For the convenience of the experiment description, these jacks are categorized into four groups marked as P_1, P_2, P_3 and P_4, as shown in Fig. 4a.

Fig. 5 demonstrates the detailed preparation process of the composite lining structure to be tested. Firstly, the outer segmental lining is assembled on a moveable plate base with wheels (see Fig. 5a and b), and then the prefabricated inner steel tube is placed inside the segmental ring by using a tower crane (in Fig. 5c). Finally, the SCC is poured into the space between the segmental ring and

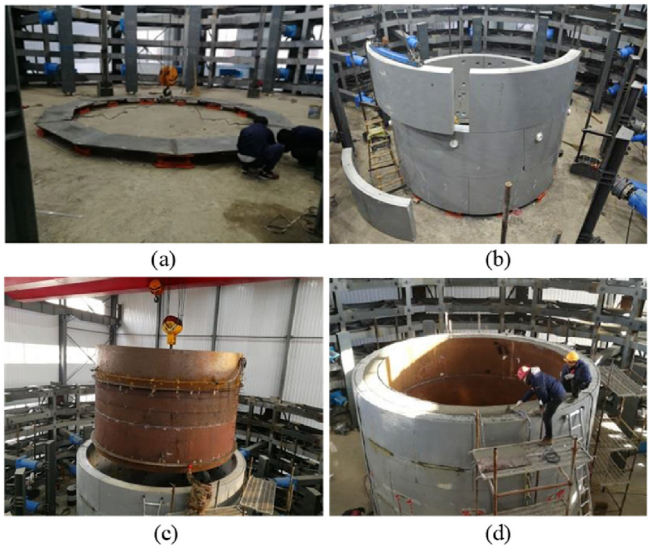

Fig. 5. Full-scale loading test set-up: (a) Movable plate base, (b) segmental ring assembly, (c) steel tube installation, and (d) self-compaction concrete pouring.

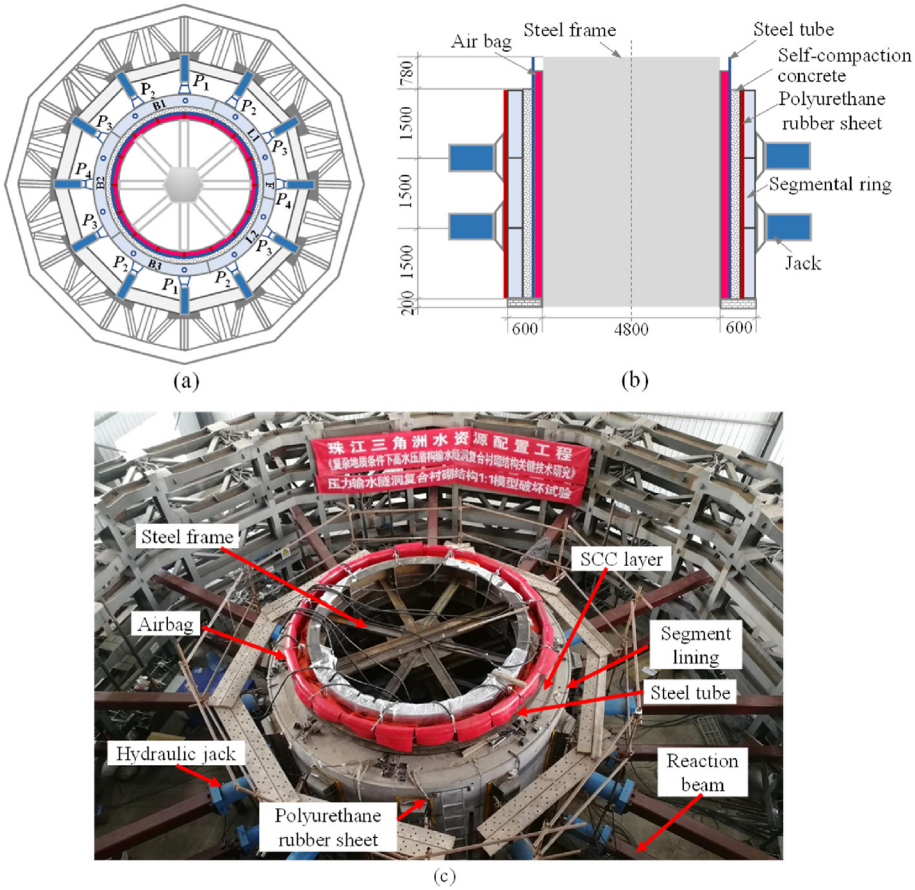

Fig. 4. Test setup: (a) Planar views of the test setup, (b) section views of the test setup (unit: mm), and (c) completed loading test setup.

steel tube and cured to the designated strength, forming a triple-layer composite lining ring (Fig. 5d). To simulate the effects of high internal water pressure, an inner reaction frame is installed, and twelve synthetic rubber airbags are uniformly placed in the gap between the inner frame and the steel tube, as illustrated in Fig. 4c. By inflating the airbags with water, a uniformly distributed pressure can be imposed on the inner surface of the steel tube. For more detailed information on simulating the internal water pressure with an airbag system, readers can refer to the work of Wang et al. (2023). Additionally, to assess the effects of studs on the mechanical behavior of the composite lining, half of the outer surface of the steel tube is fitted with studs, and the dimensions of the steel tubes and studs in this test are specified in Fig. 6.

3.2. Loading program

In this full-scale test, the loading program is divided into two stages, as illustrated in Fig. 7. At Stage 1, only the external loads are imposed by activating the hydraulic jacks (no internal pressure exerted) and the force coefficient (the ratio of P_4/P_1) was set to 0.57. Throughout this stage, the external loads are increased stepwise, and the increment of loads (between two different levels) is exerted within about 10 min until the vertical load P_1 reaches its maximum of 800 kN and the lateral load P_4 reaches 456 kN, according to the ground loading estimation of the project. The values of P_2 and P_3 are linearly interpolated between P_4 and P_1. After completing Stage 1, the external loads are progressively reduced to zero, setting the starting of Stage 2. In this second stage, the external loads are initially increased to the maximum values and remain at their peak values, and then the internal water pressure is gradually raised to its highest level of 0.8 MPa. To examine the structural responses triggered by periodic fluctuations of high internal water pressure, the internal pressures are designed to experience loading-unloading cycles three times, with the first cycle lasting 160 min and the subsequent two cycles 80 min and 40 min, respectively (see Fig. 7b).

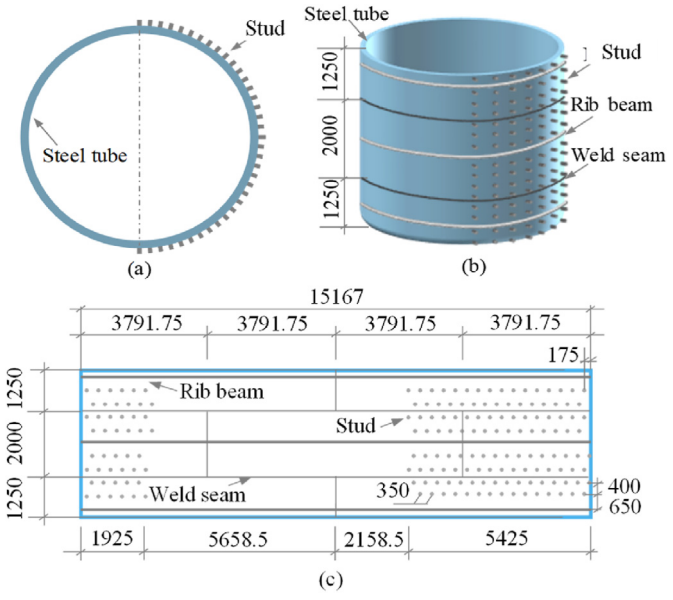

Fig. 6. Stud arrangement on the steel tube: (a) Cross-sectional view of steel tube structure, (b) schematic of steel tube, and (c) detailed drawing of steel tube extrados wall (unit: mm).

3.3. Instrumentation scheme

The steel tube, SCC, and segmental ring are integrated into a triple-layered structure in the composite lining structure. This integration involves various contacts and constraints as depicted in Fig. 8. Many interfaces between these contacts and constraints often govern the structure stability and loading capacity (Zhang et al., 2022). To gain insights into the mechanical behavior of the lining and the interaction mechanisms at these interfaces, a comprehensive monitoring scheme is implemented in the test. The instrumentation scheme, illustrated in Figs. 9 and 10, aims to record the deformation behavior of the composite lining. Furthermore, distributed fiber optic sensing (DFOS) technology is utilized in the full-scale loading tests. DFOS offers the capability to monitor distributed strain with high accuracy and has become a competent sensing tool in geotechnical monitoring which outperforms the conventional point sensors (Zhang and Broere, 2023a, b, c). When the light travels through an optical fiber, it undergoes spontaneous backscattering which results in the dispersion of light. The backscattering types can be generally classified as Rayleigh, Brillouin, and Raman scattering, while in Brillouin scattering the wavelength at which the backscattered light peaks show a linear relationship with the applied strain and temperature (Soga and Luo, 2018). This forms the basis of the working principle of a fiber optic sensing interrogator, enabling the interpretation of distributed strain and temperature data (Forbes et al., 2020). In this experimental study, the DFOS contributes to providing dense strain information for a more precise lining deformation analysis.

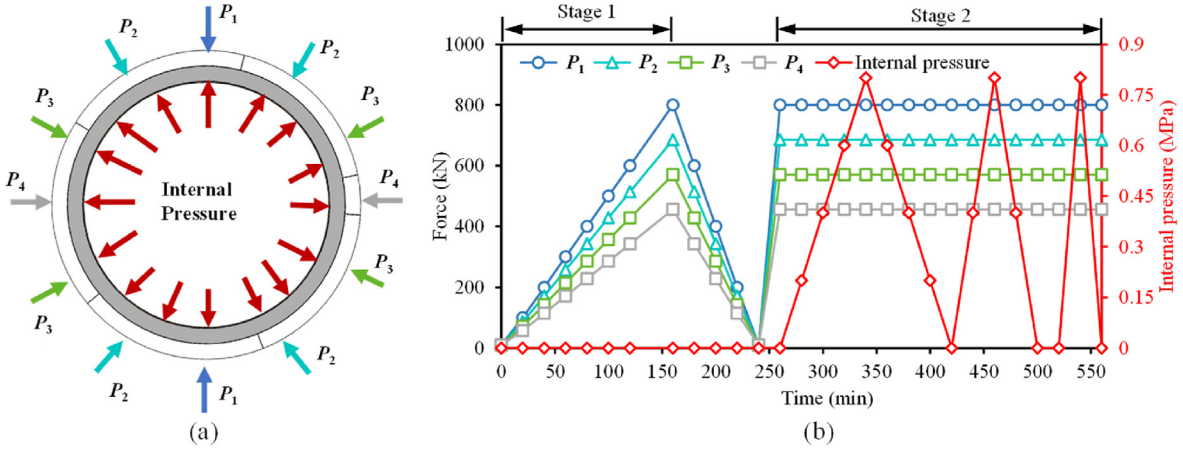

Fig. 7. Loading scheme of full-scale tests: (a) load modes, and (b) loading time-history.

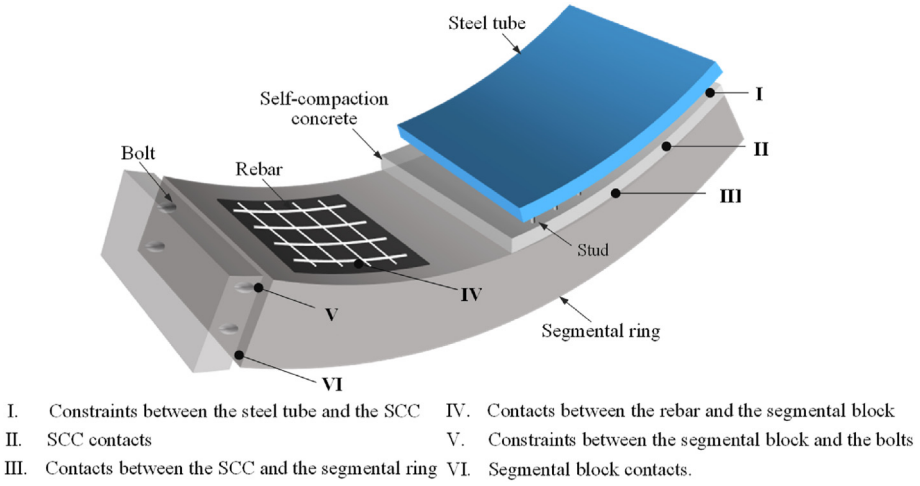

Fig. 8. Interfaces between different components.

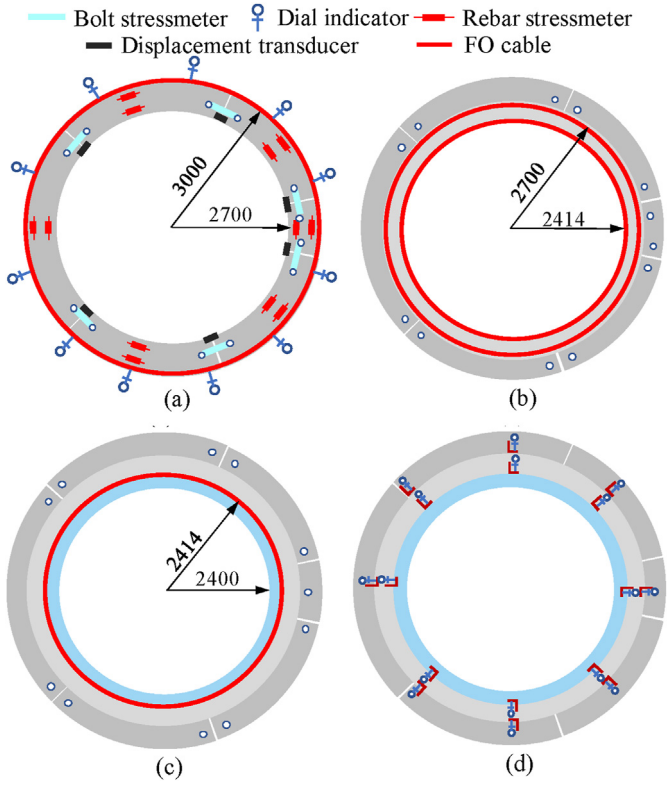

Fig. 9. Layout of the sensors instrumentation: (a) in the segmental ring, (b) in the SCC layer, (c) on the steel tube, and (d) on the inter-layer interfaces (unit: mm).

In the loading test, the following four aspects of the lining's mechanical behavior are measured and explicitly analyzed: internal forces and deformation of the segmental ring, strain development in both the SCC layer and the steel tube, and the deformation behavior of the inter-layer contact interfaces. The sensor instrumentation scheme is specified as follows:

(1) Internal forces and deformation of the segmental ring: as illustrated in Figs. 9a and 10a, the segmental ring is outfitted with one fiber optic (FO) cable continuously bonded on the lining outer surface circumferentially, and twelve rebar stressmeters are integrated into the reinforcement cage to record its deformation precisely. Within individual segment two stressmeters are placed at the extrados and intrados sides of the cross-section, and a total of six pairs (twelve) stressmeters are buried into the six segments, as shown in Fig. 9a. In addition, a total of twelve dial indicators are installed to the external circumference for monitoring the radial displacement of the segmental ring (Figs. 9a and 10b). In order to gain a deeper understanding of the interaction between segments, six stressmeters are affixed to the bolts at segment joints (Figs. 9a and 10e). Moreover, to facilitate the measurement of joint openings, a total of six high-precision linear variable differential transformer (LVDT) displacement transducers with an accuracy of ±0.01 mm is positioned to span the segment joints on the inner lining surface (see Figs. 9a and 10c).

(2) Strain developments inside the SCC layer are measured using two FO cables circumferentially placed at the outer and inner sides of the SCC cross-section. The FO cables are initially secured to discrete rods welded circumferentially to the external steel tube. Once the cables are installed, concrete is poured to fill the voids, embedding the cables within the SCC layer. This process ensures that the FO cables are tightly bonded to the SCC layer, providing reliable strain sensing.

(3) Strain measurements of the steel tube are conducted using a FO cable securely attached to its internal surface, as depicted in Fig. 9c. Prior to the cable attachment, the steel tube is meticulously cleaned using a commercial solvent. Subsequently, a fast-setting epoxy resin was employed to bond the cable to the surface firmly.

(4) The debonding displacements at the inter-layer interface within the triple-layer composite lining are measured by dial indicators. In the test, eight monitoring points (along the circumference) on the top of the lining structure are selected for characterizing the interface debonding. A dial indicator records the debonding displacement along the radius direction at each point, and both the SCC-segment and SCC-steel tube interfaces are monitored. As illustrated in Figs. 9d and 10f, the dial indicator is fitted against a special L-shaped metal piece affixed on the top surface of the composite lining.

The DFOS technology applied in this study operates based on the Brillouin optical frequency domain analyzer (BOFDA) principle and

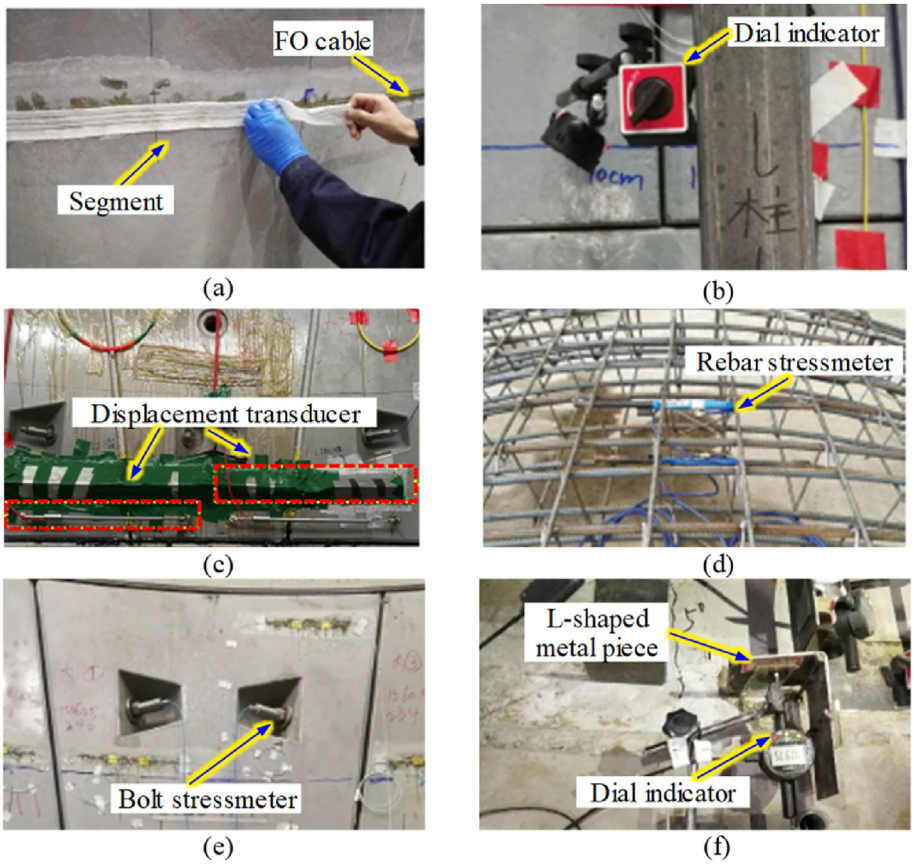

Fig. 10. Instrumentation scheme of the full-scale test: (a) FO cable on the outer segmental ring, (b) dial indicators placed circumferentially, (c) LVDT displacement transducer at segment joint, (d) rebar stressmeter on the reinforcement cage, (e) bolt stressmeter, and (f) dial indicators spanning inter-layer interface.

the type of No. fTB2505 BOFDA interrogator manufactured by fibrisTerre GmbH, Germany, is utilized for recording distributed strain data (Fibris Terre Systems GmbH, 2015), while the detailed parameters of this interrogator can be found in Table 2.

4. Results and analyses

4.1. Mechanical behavior of the SCC layer

Figs. 11 and 12 depict the strain distribution of the SCC layer during the loading process, where a negative value indicates compression while a positive value implies tension. As shown in Figs. 11a and 12a, at the initial Stage 1 when only the external loads are imposed, the SCC layer experiences compression. At a load level of $P_1 = 800$ kN, the outer side of the SCC layer displays a maximum compressive strain of -148.9 με at the 275° position, whereas the inner side manifested a maximum compressive strain of -251.9 με at the 280° position. Throughout the initial loading stage, the strain variations within the SCC layer remain minimal and far below the elastic strain limit of about -1640 με (compression) and $+95$ με (tension) of the grade C30 concrete according to the Chinese design code (GB50010-2010, 2010), indicating that the SCC layer is predominantly in an elastic state. Additionally, no observable cracking is detected at this stage.

Figs. 11b and 12b display the strain results in the SCC layer when imposing the internal pressure simultaneously at Stage 2. It can be observed that when the internal pressure reaches 0.4 MPa, tensile strain develops on the outer side of the SCC layer but remains within the range below $+95$ με, and no visible cracks are detected in the structure. Moreover, the strain distribution of the SCC layer on the right side of the cross-section is relatively uniform, indicating that the studs placed on the right side have improved the deformation compatibility of the concrete. As the internal pressure increases to 0.6 MPa, the maximum measured strains on the outer and inner sides are $+133$ με and $+241$ με, respectively. Besides, a loud abnormal noise is emitted according to test recordings, which may imply the cracking initiation within the SCC layer. A further increase of the internal pressure to 0.8 MPa leads to a rapid expansion of the cracks within the SCC layer. The cracks first occur in the SCC layer close to the crown and spring areas. At an internal pressure of 0.8 MPa, about nine continuous cracks are observed from the top of the cross-section of the composite lining structure, and the most significant cracks are observed at the positions of 144° and 345°, with maximum widths of 0.37 mm and 0.67 mm,

Table 2
Parameters of the BOFDA interrogator.

Maximum measuring distance (km)	Strain measurement accuracy (με)	Minimum spatial resolution (cm)	Maximum sampling resolution (cm)	Sampling frequency range (GHz)	Strain range (%)
25	±2	20	5	9.9–12.0	−1.5 - +1.5

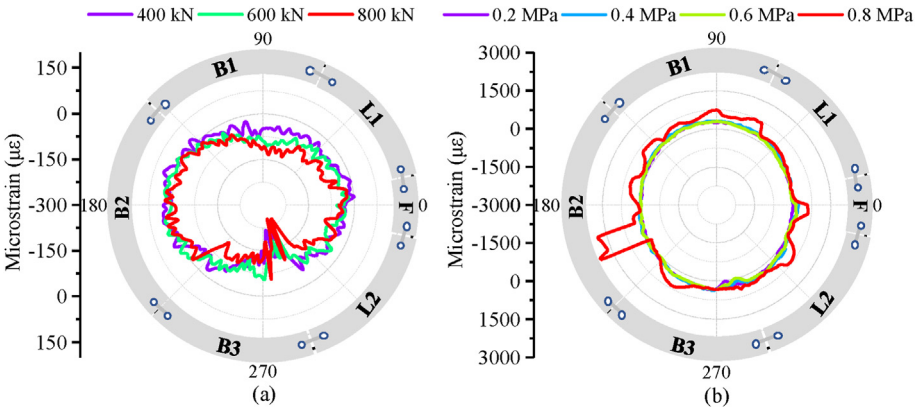

Fig. 11. Strain distribution of the outer side within the SCC layer at loading (a) Stage 1, and (b) Stage 2.

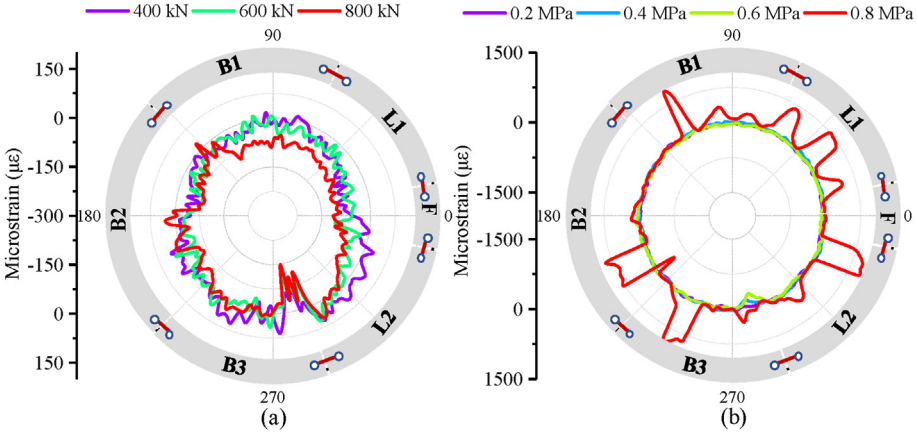

Fig. 12. Strain distribution of the inner side within the SCC layer at loading (a) Stage 1, and (b) Stage 2.

respectively (see Fig. 13). From the strain distribution within the SCC layer, the cracks on the right side of the cross-section are relatively evenly distributed, indicating that the studs enhance the deformation compatibility of the concrete. Notably, at the end of the loading Stage 2 when the internal pressure has experienced three loading-unloading cycles, crack evolution tends to stabilize and no additional cracks forms in the SCC layer. This phenomenon suggests that the cracks mitigate the load proportion in the SCC layer and transfer the internal pressure to the segment layer under the periodic internal pressure variation.

4.2. Mechanical behavior of the segmental ring

In the loading tests, FO cable is circumferentially bonded on the external surface of the outermost segmental lining and monitors the distributed strain information. Fig. 14 depicts the strain evolution on the segmental ring during the tests, with a positive value indicating a tensile status. At Stage 1, when no internal pressure is imposed, the entire cross-section mostly experiences compression mostly. Specifically, upon applying the maximum external forces level ($P_1 = 800$ kN), the compressive strain near the joint between segments B2 and B3 increases significantly to -521 με, while only a tension strain of $+68$ με is detected at the position of 78°. In a similar vein, the strain of segment L1 is also recorded to show a local peak strain of about -341.7 με. According to the Chinese design code of concrete structures (GB50010-2010, 2010), for C55 grade concrete the designated elastic limit of compression and tensile strains are -1725 με and $+112$ με, respectively. Therefore, the average value for each segment at Stage 1 is below the allowable limit for compressive strain specified by the standards (see Fig. 14d), indicating that the structure is in the elastic deformation stage.

At loading Stage 2, as the internal pressure gradually increases, the compression strain on the segment ring is gradually mitigated until most cross-sections exhibit a tension status. The compression strain is mitigated when the internal pressure is at 0.2 MPa and 0.4 MPa. Still, not that significant, and the maximum compression strain is about -407 με at position of 215°. In comparison, a maximum tension of $+105$ με is measured at the position of 342°, indicating that the segment ring is still in an elastic state. However, with the internal pressure being increased to 0.6 MPa, a maximum tension of $+206$ με is monitored at segment B3 (in Fig. 14e), which is highly above the tensile limit ($+112$ με) of the concrete, and this may indicate the evolutions of tensile cracking within the segments. The tensile strain further increases to about $+219$ με at the pressure of 0.8 MPa, which implies the potential further development of cracking. In addition, with the cross-section, the area experiencing compression is still significant, mainly occurring at the area of 0°–70° and 180°–234°, which implies that the lining is still under compression partially at the internal pressure of 0.8 MPa.

According to the strain distribution of the segmental lining in Fig. 14b, the tension area mainly concentrates on the areas left to the crown and right to the tunnel bottom. This manifests as compressive strains on both sides of the lining while the crown area undergoes tension, suggesting an inclined ovalization of the ring as shown in Fig. 14c. Considering that vertical load dominates in external force sequence ($P_1 > P_2 > P_3 > P_4$), the crown near P_1 exhibits a higher

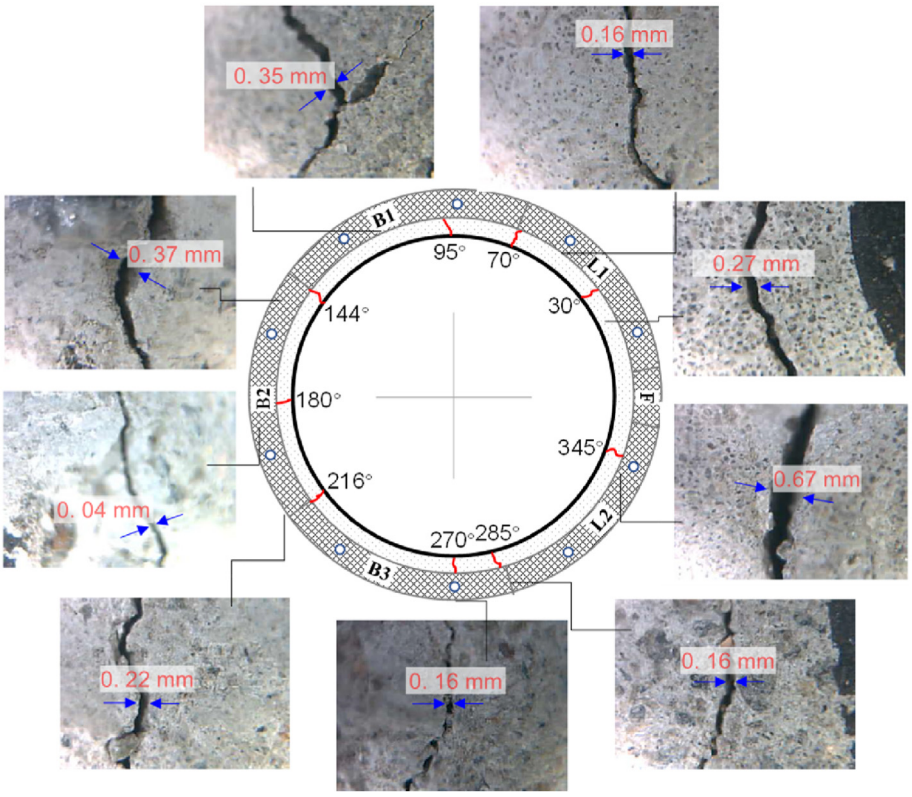

Fig. 13. Crack development in the SCC layer at the end of the second load-unload cycle.

propensity for deformation compared to the sidewalls. Moreover, due to the presence of the studs, the asymmetric deformation of the SCC layer further influenced the strain distribution characteristics of the outer segmental lining. From these analyses, it is recommended that in the future structural health monitoring of the actual water conveyance tunnel, locations of the B1-L1 and B2-B3 joints should be paid more attention due to their pronounced deformation concentrations. In addition, to ensure the stability and longevity of the segmental ring, it is important to optimize its structural and waterproof designs considering the serviceability assurance of these deformation-prone regions.

Fig. 15 presents the segmental ring's internal stress and radial displacements during the loading Stage 1. As shown in Fig. 15a, the rebar stresses are generally very low, with a maximum compression and tension of −14.7 MPa and +1.94 MPa, respectively, which is far below the rebar stress limit of 400 MPa. The behaviors of the rebars are consistent with the deformation pattern observed in the SCC layer during the tests. It can be inferred from Fig. 15b that when under external forces only, the overall cross-section is predominantly under compression, but when the external forces increase, partial of the segment lining displaces outwardly (see the area of 145°—180°), which causes tension within the segment as demonstrated in Fig. 14c. The vertical convergence deformation of the segmental ring is more significant than the horizontal convergence since the vertical forces P_1 is larger than the horizontal forces P_4. The maximum values of measured rebar stress and radial displacement are considered for further analysis of the segmental lining deformation. Notably, both the maximum rebar stress and the maximum radial displacement increase with the applied external loads, but the first load step (from 0 to 100 kN) triggers the highest stress and radius displacement increments. Afterward, the maximum rebar stress shows a highly linear relation with the loads, implying the elastic state of the segmental lining.

The segmental joint openings at the inner surface are presented in Fig. 16a, where a positive value indicates a joint opening, while a negative value indicates a joint closure. It shows that the joint openings generally increase with the external loads but are quite insignificant overall. Specifically, when the external force P_1 reaches 800 kN, the maximum observed joint opening amounts to only 0.03 mm at the joint B3-L2. Fig. 16b displays the bolt stress variations results. Notably, the bolt stressmeter at joint B3-L2 is damaged, and therefore the most significant bolt stress variation is recorded at joint B1-B2 (see Fig. 16b). According to the bolt stress results, the bolt at joint B1-B2 experiences further compression. In contrast, the bolts at joints B2-B3, L2-F, and L1-F exhibit tension, indicating a tendency for joint opening.

The monitoring results of point sensors throughout the loading Stage 2 are demonstrated in Fig. 14. Fig. 17a illustrates how bolt stresses vary with the increasing internal pressure while the external loads remain at the peak values. The bolt stresses do not show significant variation during the initial loading phase from 0 to 0.4 MPa. However, upon reaching an internal pressure of 0.4 MPa, the stresses of two bolts (at joints B1-B and L2-F) significantly increase. The significant stress variation is identified on the bolt at the joint B1-B2, registering a stress value of 364 MPa when the internal pressure escalates from 0.4 MPa to 0.8 MPa. Notably, except for the bolt stresses at joints B1-B and L2-F, the bolt stress of the other three joints does not show significant variations. Fig. 17b demonstrates a gradual increase in the axial stress of the rebars located in the intrados sides of segmental ring with rising internal water pressures. Notably, as the internal water pressure approaches 0.6 MPa, the axial stress of the rebars increase rapidly and the axial stress of the rebars in segments B1, B2, and B3 suffer a larger proportion of internal water pressures. Observations suggest that the outermost segmental lining bears the brunt of the internal water pressures, leading to localized damage once cracks appear in the

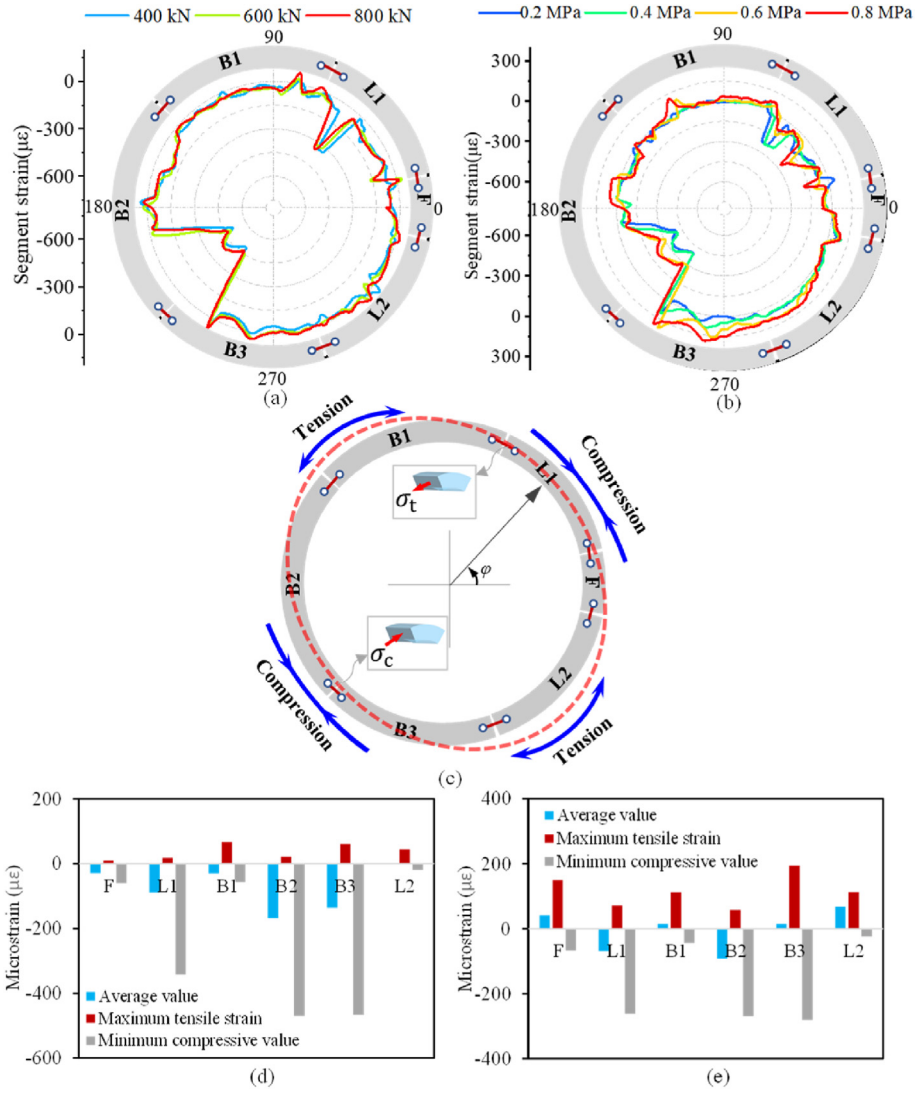

Fig. 14. Strain distribution of segmental lining at (a) Stage 1, and (b) Stage 2, (c) deformation pattern of the segmental lining, and (d) and (e) comparison of local strains with average strains at 800 kPa and 0.8 MPa.

SCC layer. As depicted in Fig. 17a and b, the peak stresses of the bolts are recorded as 418.13 MPa, 438.53 MPa, and 441.65 MPa, respectively. Conversely, the stresses on the internal rebars within the segments show a decreasing trend, indicated that the rebars have excellent load-bearing performance during the cyclic loading stage. Based on the data and the work of Zhou et al. (2022), the primary damage to the segmental lining is observed to concentrate on the joint area throughout the periodic loading phase. This vulnerability is primarily attributed to the redistribution of internal forces stemming from cracks in the SCC layer. Nonetheless, the loading test demonstrates that the composite lining structure can still bear the internal water pressure even after local damage occurs. Accordingly, it can be inferred that the composite lining can maintain normal serviceability even when subjected to the fluctuation of high internal pressure.

The joint openings and radial displacements of the segmental ring during cyclic loading are plotted in Fig. 17c and d. The joint opening increases gradually with internal pressure, and the joint B1-B2 presents the most significant deformations, reaching a maximum of about 1.2 mm at the pressure level of 0.8 MPa in the first cycle. However, only three of the six joints exhibit significant joint openings, namely the joints B1-B2, L2-F and F-L1, and this implies the internal pressure causes non-uniform joint openings along the ring circumference. Particular attention should be given to joints B1-B2 in future field monitoring, as they exhibit the most significant joint openings and are therefore more susceptible to risks of opening and leakage. Furthermore, in the SCC layer, pronounced penetrating cracks are more likely to develop near these joint locations (see Fig. 13) when the internal pressure exceeds 0.6 MPa. Additionally, the rapid increase in bolt stresses in Fig. 17a suggests that the segmental ring subsequently bears greater loads. Given the multiple interfaces in composite tunnel lining, the deformation behavior of the segmental ring diverged from that of the single-layer lining, as detailed in Zhang et al. (2019). According to the radial displacement results in Fig. 17d, both sides of the segmental lining are under compression, while the tunnel crown and invert experience tension, and this suggests that the composite lining cross-section deforms into an inclined elliptical shape. However, it should be noted that the joint openings are within a small range, say about 1.2 mm at the first peak and 0.7 mm at the second and third peak as shown in Fig. 17c, which is below the stipulated limit of 2 mm according to the tunnel construction code

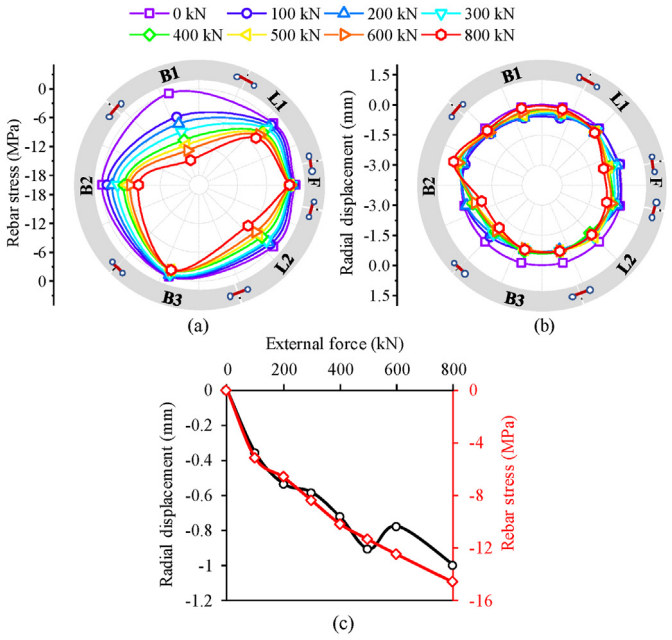

Fig. 15. Monitoring results of (a) rebar stress, (b) radial displacement, and (c) the maximum values of rebar stress and radial displacement versus external loads.

(GB 50446-2017, 2017). Therefore, the composite lining performs with sufficient safety under the fluctuation of high internal pressure.

4.3. Mechanical behavior of steel tube

Fig. 18 shows the strain development of the steel tube during the tests. From the strain profile, it can be observed that during Stage 1, the entire section is predominantly under compression, exhibiting a symmetrical deformation pattern across the cross-section. This suggests that the impact of the studs on the deformation of the steel pipe is minimal, particularly when the external pressure P_1 is below 800 kN. In addition, the peak compressive strains are observed at locations of 90° and 270°, proximate to the lining crown and invert. At loading Stage 2, it is found that when the internal pressure exceeds 0.5 MPa, the strain signal sampled by the FO cable is notably impacted, and therefore only data ranging from 0.2 MPa to 0.5 MPa are chosen for analysis in this study. When the

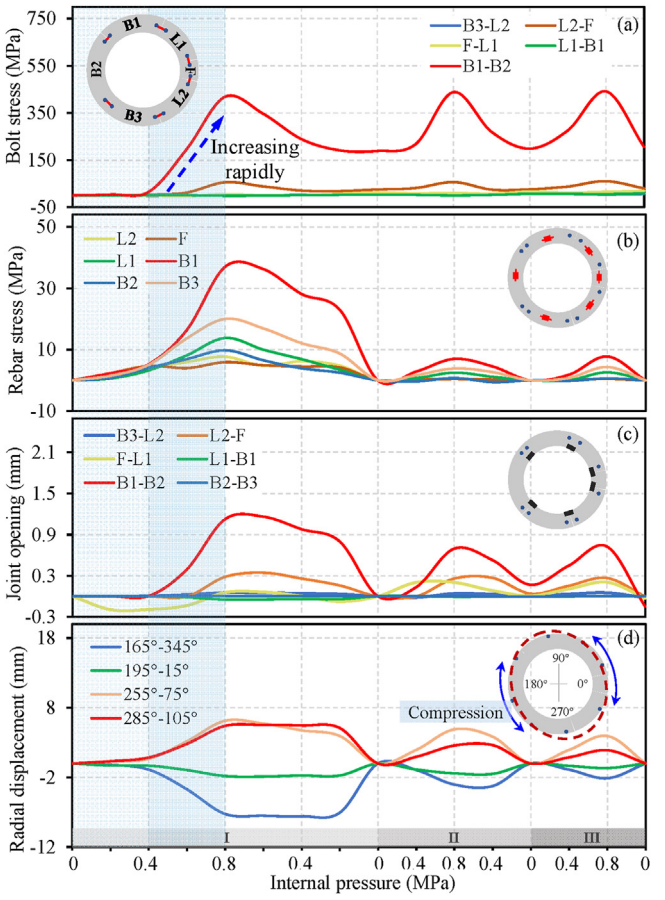

Fig. 17. Monitoring results of (a) bolt stresses, (b) rebar stresses, (c) joint opening, and (d) radial displacement in the cyclic loading Stage 2.

internal pressure rises to 0.2 MPa, the strains at the lining crown and invert are recorded to increase by 59 με and 64 με, respectively. By the time the internal pressure reaches 0.5 MPa, conspicuous tensile strains are recorded by the FO cable, indicating a significant expansion tendency in the steel tube, but the strains of the steel tube are far below the material's elastic limit of 295 MPa.

According to the afore analyses, the structural behaviors of the triple-layer composite tunnel lining are summarized as follows:

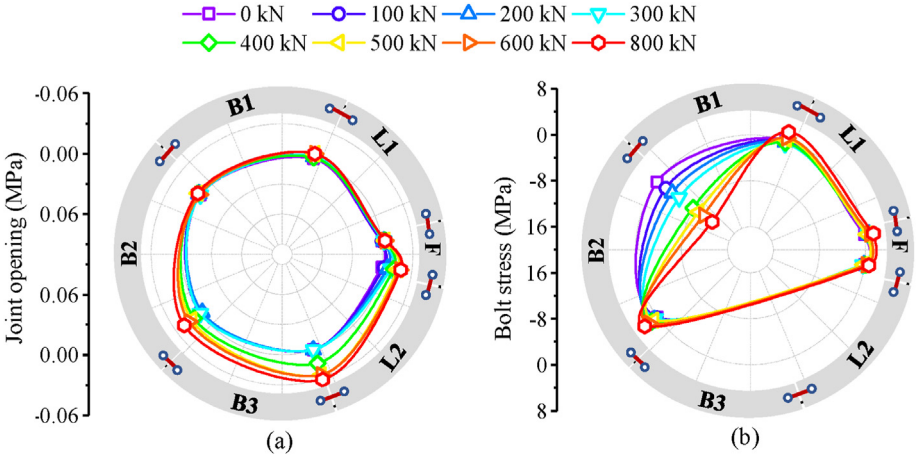

Fig. 16. Monitoring results of (a) joint openings, and (b) bolt stresses.

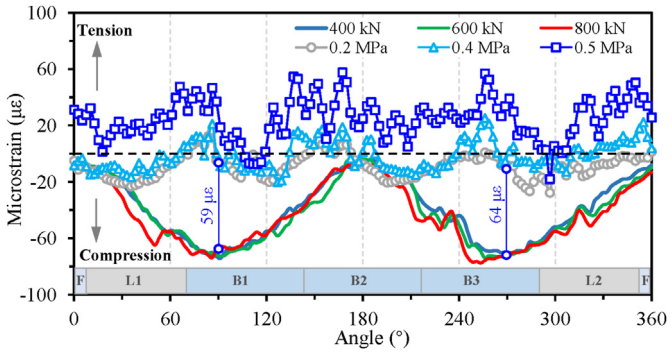

Fig. 18. Strain development on extrados surface of steel tube.

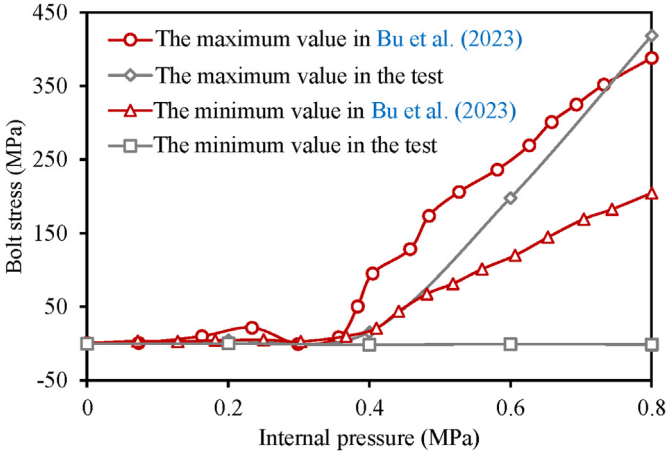

Fig. 20. Development of bolt stress in different types of tunnel linings.

initially, the composite lining structure is in a state of elasticity during the external loading stage, and the whole cross-section is predominantly under compression. Subsequently, when the internal pressures are imposed and increased gradually, the SCC layer exhibits significant tension until reaching the tensile strength (when the pressure reaches above 0.4 MPa), triggering visible cracks that mainly concentrate on the area near the segmental joints. Finally, when the internal pressure reaches its maximum level of 0.8 MPa, nine major cracks penetrate the SCC layer along the radial direction. At these cracking locations, the SCC layer loses its axial bearing capacity under the internal pressure, transferring the load to the segmental lining and the steel tube. During the tests, the steel tube behaves elastically under the impacts of both external loads and internal pressures, and this proves that the steel tube plays a critical role in preventing water leakage during the operation phase. The presence of studs enhances the load-bearing capacity of the SCC layer and influences the local deformation pattern of the segmental lining, but their effect on the deformation of the steel pipe is minimal. In the single-layer lining structure, cracks are likely to occur during the external pressure loading phase, predominantly appearing at the side waist segment B3 (see Fig. 19a). In the double-layer lining structure, the inner concrete layer is more susceptible to cracking under internal pressure, with a significantly higher number of cracks compared to the triple-layer lining structure (see Fig. 19b). Moreover, the strain distribution of the connecting bolts reveals that in the triple-layer lining structure, only the bolts at positions B1 and B2 show a noticeable increase in internal force, which remains smaller than the corresponding increase in the double-layer lining structure (see Fig. 20). Overall, the full-scale loading test demonstrates that the triple-layer composite lining maintains high serviceability under fluctuating high internal pressure, despite localized damage occurring in the SCC layer.

4.4. Mechanical behavior of inter-layer contact face

Fig. 21 depicts the variations in debonding displacement at the interfaces of the segment ring, SCC layer, and inner steel tube during the external loading Stage 1. Herein, the negative value indicates compression at the interface, whereas the positive value denotes a debonding (separation). As the load increases, the debonding displacement at the interfaces also grows. At an external load of $P_1 = 800$ kN, the debonding displacement between the segment ring and SCC is measured to be 0.096 mm at the 0° position, yet no debonding is detected at 185° position. In contrast, the

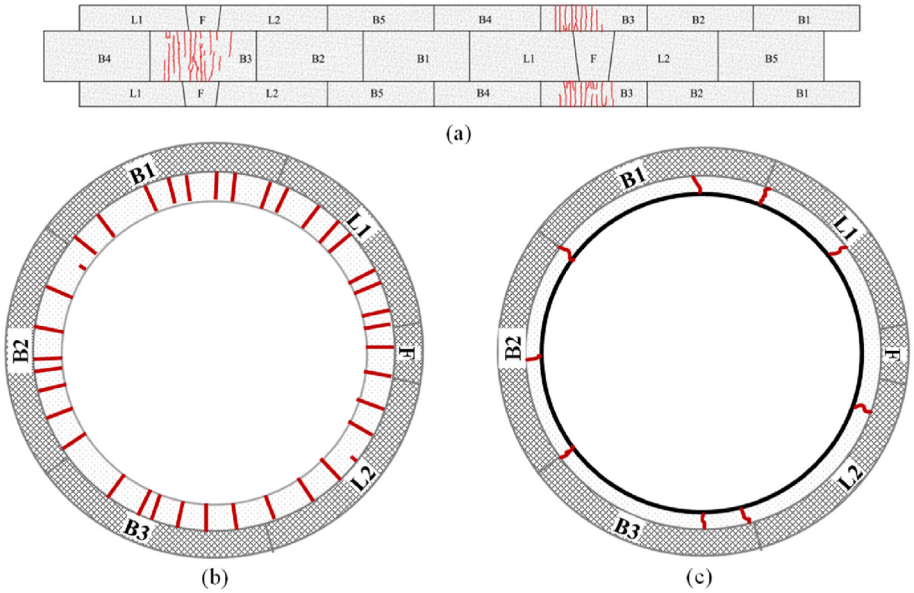

Fig. 19. Crack distribution on the concrete lining layer in the study by (a) Zhang et al. (2019), (b) Bu et al. (2023), and (c) the model test (Cracks are indicated by red lines).

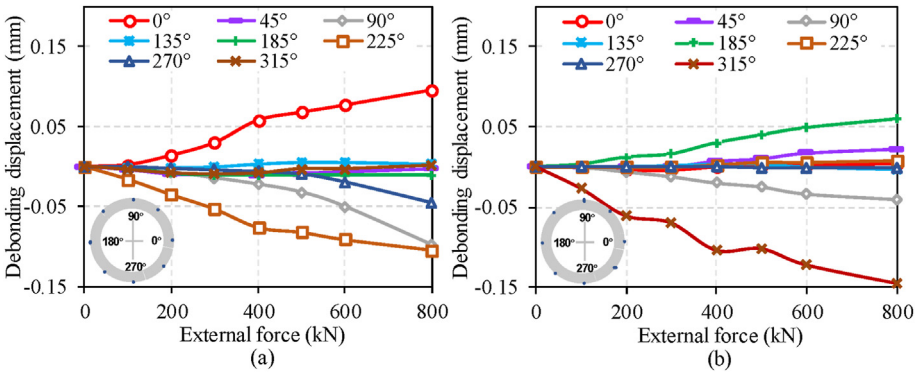

Fig. 21. Development of debonding displacement between (a) segment ring and SCC, and (b) SCC and steel tube.

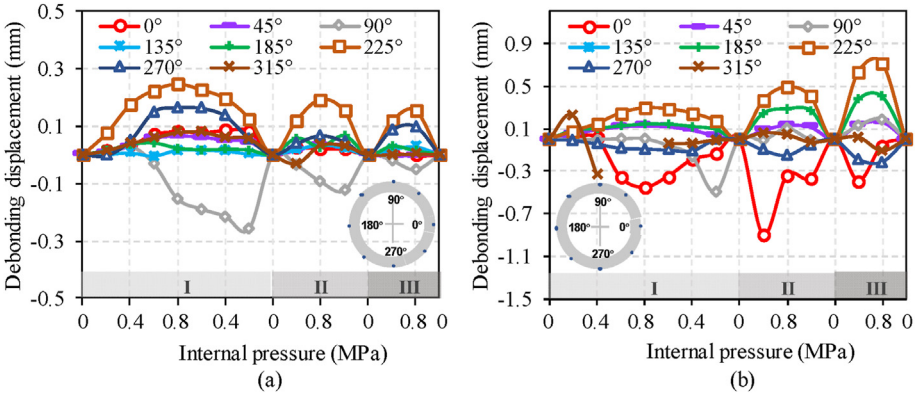

Fig. 22. Development of debonding displacement between (a) segmental ring and SCC; (b) SCC and steel tube under the periodic loading.

debonding displacement between the SCC and steel tube was 0.06 mm at 185°, notably greater than the slight debonding displacement of +0.004 mm observed at 0°. These differences in the debonding behaviors can be primarily attributed to the arrangement of studs on the steel tube, which strengthens the bond between the steel tube's extrados surface and the SCC layer. However, the existence of studs expands the debonding displacement between the segment ring and SCC layer, especially on the right half of the cross-section.

Fig. 22 depicts the variations of debonding displacement at the segment-SCC and steel lining-SCC interfaces under the impact of internal pressure at Stage 2. During the three loading-unloading cycles, as the internal pressure reaches 0.8 MPa, the debonding displacements of the segment-SCC interface at 225° are successively measured about +0.244 mm, +0.191 mm, and +0.153 mm (in Fig. 22a), which are larger than corresponding values at the 0° (i.e., +0.086 mm, +0.025 mm, and +0.08 mm, successively). Similarly, the maximum debonding displacements between the SCC and steel tube are recorded at the 225° position, registering values of +0.295 mm, +0.49 mm, and +0.717 mm successively (in Fig. 22b). The SCC-steel tube interface at the 0° position is in alternating tension-compression state and the debonding displacements are −0.063 mm, −0.005 mm, and +0.186 mm, respectively. Hence, the studs on the steel tube intensify the bonding strength between the SCC and the steel tube, and influence the interaction between the SCC and the segmental lining. Consequently, under cyclic loading, the left side of the lining structure exhibited greater debonding displacements. However, due to the existing cracks in SCC layer, the debonding displacements between the SCC and steel tube gradually accumulate along with the cyclic loadings. Notably, the debonding between the SCC and steel tube will increase the possibility of groundwater infiltration, further boosting the likelihood of steel corrosion and negatively impacting the structural integrity. Therefore, it is recommended that proper sealing measures should be taken, such as installing external synthetic membranes between the segment and SCC layers to prevent water infiltration.

5. Assessment of structural behavior

To quantitatively assess the changes in the mechanical performance of composite lining structure, structural bearing scale factor (β) is proposed to analyze the loading distribution in the triple-layer linings, which can be expressed as

$$\beta_i = \frac{N_i}{\sum_{i=1}^{n} N_i} \tag{1}$$

where β_i is the bearing scale factor of each layer (here β_1, β_2 and β_3 are the bearing scale factor of the steel tube, SCC, and segmental lining); and N_i is the axial force of each layer (here N_1, N_2 and N_3 are the axial force of the steel tube, SCC, and segmental lining, respectively).

For the steel tube, σ_1 is assumed to be uniformly distributed along the cross-section. N_1 is acquired by

$$N_1 = \sigma_1 A_s = \varepsilon_1 E A_s \tag{2}$$

where A_s is the cross-sectional area of the steel tube, ε_1 is the

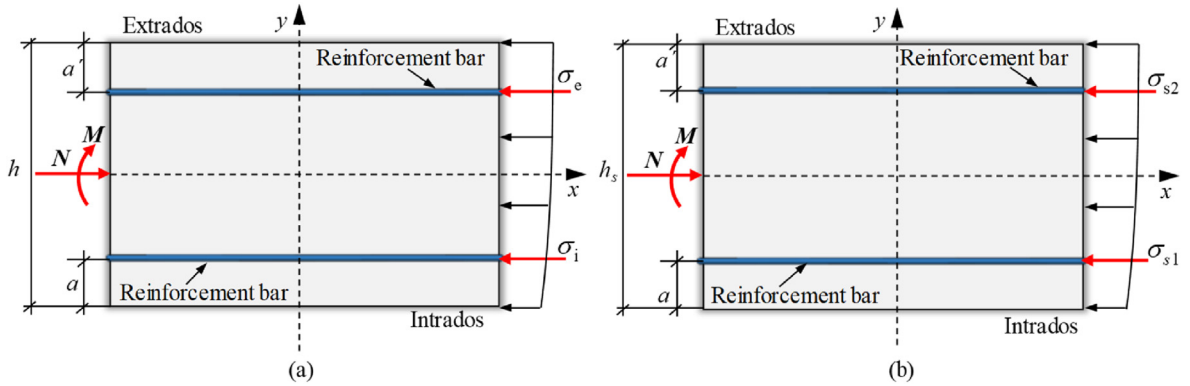

Fig. 23. Stress state analyses of (a) SCC, and (b) segmental lining.

measured strain of FO cable, and E is the elastic modulus of the steel tube material.

As shown in Fig. 23a, for the SCC, the axial force N_2 is estimated based on the method proposed by Bilotta and Russo (2013) and expressed as

$$N_2 = E_c A_c \frac{\varepsilon_i\left(\frac{h}{2}-a'\right)+\varepsilon_e\left(\frac{h}{2}-a\right)}{h-a-a'} \tag{3}$$

where E_c is the elastic modulus of concrete; A_c is the cross-sectional area of the concrete layer; ε_i and ε_e are the measured strains of FO cables installed on the intrados and extrados of SCC, respectively; h is the thickness of SCC; a and a' are the thickness of the inner and outer protective layers for reinforcement bars, respectively.

Subsequently, the axial force N_3 of segmental lining is evaluated by (Zhou et al., 2017):

$$N_3 = 1000(1-250C)Cf_c b h_s - \frac{62500}{3} f_c b h_c{}^3 \tan^2\alpha + E_s\varepsilon_{s1}A_{s1} + E_s\varepsilon_{s2}A_{s2} \tag{4}$$

$$C = \varepsilon_{s1} + \left(\frac{h_s}{2}-a\right)\tan\alpha \tag{5}$$

$$\tan\alpha = \frac{\varepsilon_{s2}-\varepsilon_{s1}}{h_s-a-a'} \tag{6}$$

where E_s is the elastic modulus of the reinforcement bar; f_c is the compressive strength of concrete; b is the width of the lining segment; h_s is the thickness of the segment; A_{s1} and A_{s2} are the cross-sectional area of reinforcement bars on the intrados and

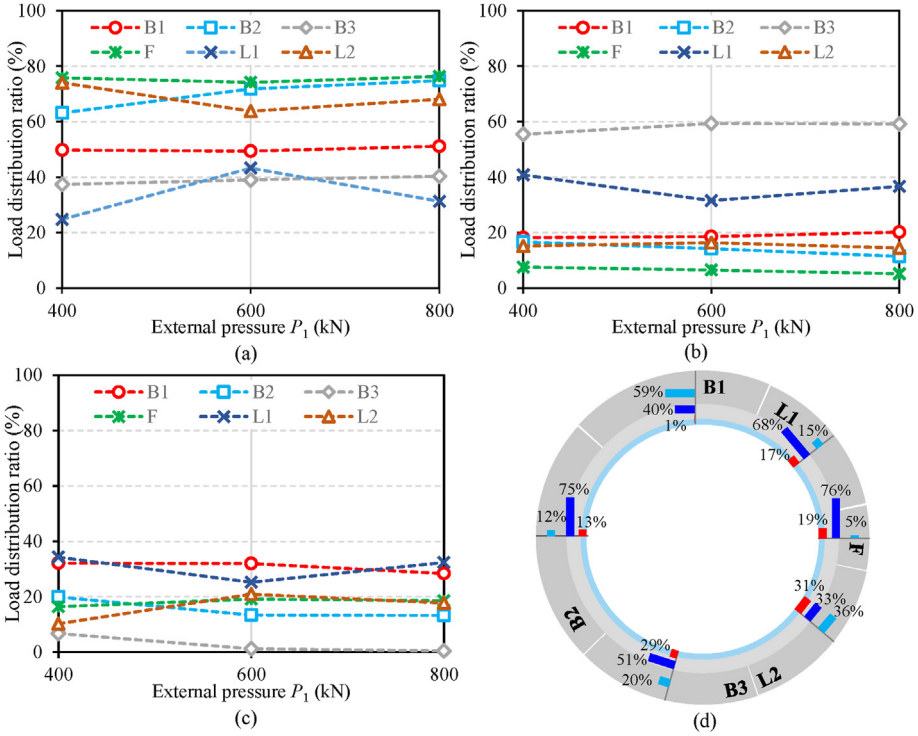

Fig. 24. Variations of the structural bearing scale factor (β) for (a) SCC, (b) segmental lining, (c) steel tube in the external loading stage, and (d) distribution of structural bearing scale factor for triple layer lining with an external load of 800 kN.

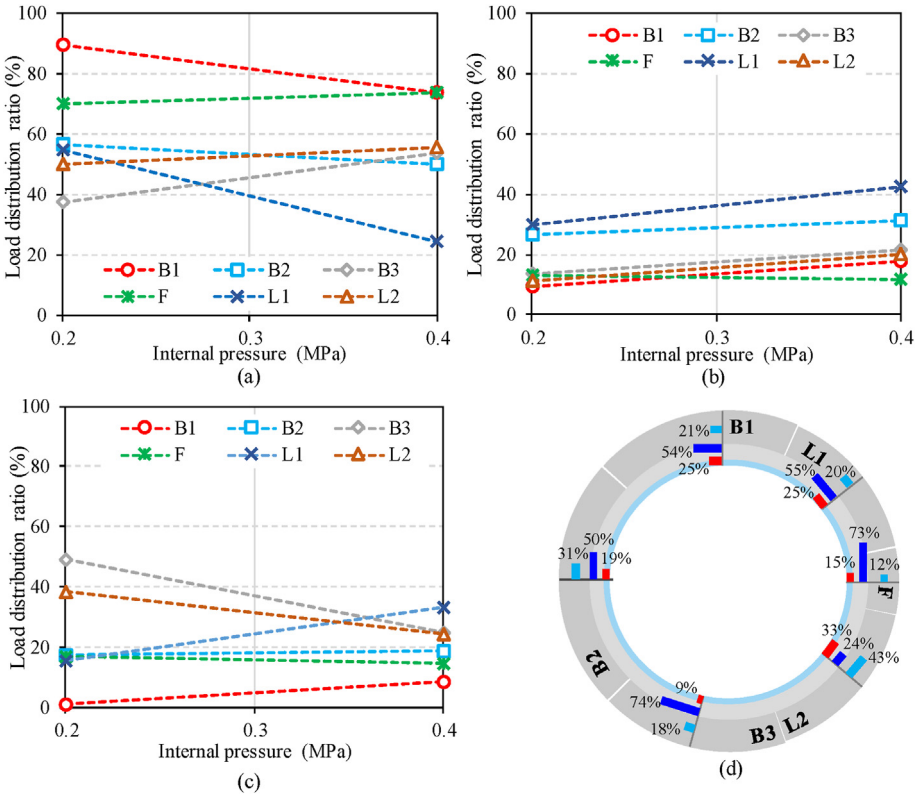

Fig. 25. Variations of the structural bearing scale factor (β) for (a) SCC layer, (b) segmental lining, (c) steel tube in the external loading stage, and (d) structural bearing scale factor for triple-layer lining to an internal pressure of 0.4 MPa.

extrados of segment cross-section, respectively; and ε_{s1} and ε_{s2} are the measured strains by the rebar stressmeters installed on the intrados and extrados of the individual segment, respectively.

Fig. 24a–c presents the variations of β values for the triple-layer lining structure under different levels of external load only. It is evident that, as the external load increases, the SCC layer in the composite lining structure bears the highest proportion of the load, while the steel tube layer exhibits the smallest proportion. With an increase in the external load, the β values of the SCC layer slightly increase, whereas those of the segmental lining and steel tube layers decrease. When the external load P_1 reaches its maximum value of 800 kN, the β values for the SCC layer, segmental lining, and steel tube are 58%, 23%, and 19%, respectively. According to Fig. 24d, a notable observation is that the β values of the SCC layer and steel tube layer on the right side of the structure are significantly greater than those on the left side, while the segmental lining layer shows the opposite characteristics. This disparity is attributed to the arrangement of studs on the outer surface of the steel tube in the right half of the structure, reinforcing the cohesion between the steel tube and the intermediate SCC layer and resulting in a higher load-sharing on the right side of the cross-section.

Fig. 25 illustrates the variations of the β values for the triple-layer lining structure as the internal pressure level gradually increases. Since the SCC layer exhibits cracking when the internal pressure reaches 0.6 MPa, indicating a loss of its ability to withstand the internal pressure, only the β values corresponding to the internal pressures below 0.4 MPa are analyzed herein. When the internal pressure reaches about 0.2 MPa, the SCC layer predominantly undertakes the internal pressure, and the β values of the segmental lining and steel tube are relatively similar. As the internal pressure increases to 0.4 MPa, the β values of the SCC layer and steel tube decrease while those of the segmental lining increase. However, it should be noted that the SCC layer still serves as the main load-bearing structure during the internal pressure loading process. Notably, due to its higher capacity to withstand internal pressure, the SCC layer is susceptible to cracking as the internal pressure rises, making it a vulnerable part of the composite lining structure. Fig. 25d illustrates that the values of the triple-layer lining show a significant difference in the left-bottom region, specifically near Segment B1. When the internal pressure remains below 0.4 MPa, the SCC layer predominantly bears the internal pressure in this region, making it the most prone to cracking. Once the cracks emerge in this area, the β values of the segmental lining significantly increase, causing a sharp stress increase in the joint bolts between segments B1 and B2 that may further yield in the subsequent loading process. This implies both the outermost segmental lining and SCC layer are prone to excessive deformation which may deteriorate the performance of the composite lining. In contrast, the steel tube behaves in elastic status throughout the whole loading process, and consequently, it functions as the ultimate load-bearing structure for high internal pressure, as well as for assuring water-tightness and serviceability of the tunnel in future operation.

6. Conclusions

The present study conducts full-scale tests on the triple-layer composite lining of a mega water conveyance tunnel, which is composed of the outermost segmental lining, self-compaction concrete (SCC) layer and an inner steel tube, to investigate its mechanical behaviors and deformation patterns under normal serviceability state. A unique airbag loading system is developed and applied to impose uniformly distributed internal pressures in this test. The mechanical behaviors of the composite lining under

external loads and combined external and internal loads are specifically investigated. The main conclusions are as follows:

(1) Under the maximum vertical loads of 800 kN and horizontal loads of 453 kN, the composite lining behaves overall in an elastic status, and the monitored deformations (lining strains and joint displacements) and stresses (rebar and bolt stresses) are generally within a small range below the elastic limits of materials.
(2) Under combined external loads (at peak levels) and increasing internal pressure, the overall compression deformation developed in the composite lining is mitigated. The composite lining maintains a high elasticity when the internal pressure is below 0.4 MPa. However, cracks initiate within the SCC layer when the internal pressure exceeds 0.4 MPa. At the peak level of 0.8 MPa, the occurrence of several penetrating cracks in the SCC layers causes a redistribution of internal forces within the composite lining.
(3) The cracks in the SCC layer tend to concentrate on the segmental joints, indicating that the discontinuity of the segmental ring significantly influences the overall behavior of the composite lining. These joint locations are therefore more susceptible to deformation, warranting greater attention in structural health monitoring during the service phase of future projects.
(4) The configuration of studs on the steel tube-SCC interface can effectively strengthen the interface bonding and significantly reduce the debonding tendency while at the cost of increasing the debonding tendency at the SCC-segment interface. However, the strengthening effects of the studs are compromised by the occurrence of cracks in SCC layers.
(5) Overall, the triple-layer composite lining can maintain high serviceability performance under the impacts of cyclic fluctuation of high internal pressures despite the local damages occurring in the SCC layer, since the monitored stresses and deformations generally indicate within the allowable strength limit of materials.

However, one limitation of this study is the inability to fully replicate the complexity of actual engineering environments, where ground loads vary significantly due to different geological conditions. This restricts the accuracy of the findings when applied to field scenarios. To address the challenges, a structural health monitoring system should be implemented in field to provide real-time monitoring and a detailed evaluation of the tunnel structural condition.

CRediT authorship contribution statement

De-Yang Wang: Writing – original draft, Investigation, Formal analysis. **Hong-Hu Zhu:** Writing – review & editing, Supervision, Conceptualization. **Xue-Hui Zhang:** Writing – review & editing, Supervision. **Jing-Wu Huang:** Project administration, Investigation. **Zhen-Rui Yan:** Resources, Project administration, Investigation. **Dao-Yuan Tan:** Writing – review & editing, Supervision. **Shao-Qun Lin:** Investigation, Data curation.

Declaration of competing interest

The authors declare that they have no known competing financial interests or personal relationships that could have appeared to influence the work reported in this paper.

Acknowledgments

This work was financially supported by the National Natural Science Foundation of China (Grant Nos. 42225702 and 42077235) and Special Research Foundation on Water Resources Allocation Project in the Pearl River Delta (Grant No. CD88-QT01-2022-0085). We thank B. Wu, J. Wang, and W.Z. Yu, all of Nanjing University, for their assistance in date analyses.

References

Ahad, Z., Kaveh, A., 2018. The effect of topography on stability of shallow tunnels case study: the diversion and conveyance tunnels of Safa Dam. Transp. Geotech. 14, 126–135.
Armaghani, D.J., Koopialipoor, M., Marto, A., Yagiz, S., 2019. Application of several optimization techniques for estimating TBM advance rate in granitic rocks. J. Rock Mech. Geotech. Eng. 11 (4), 779–789.
Bilotta, E., Russo, G., 2013. Internal forces arising in the segmental lining of an earth pressure balance-bored tunnel. J. Geotech. Geoenviron. Eng. 139 (10), 1765–1780.
Blom, C.B.M., 2002. Design Philosophy of Concrete Linings for Tunnels in Soft Soils. Delft Univ. of Technology, Netherlands, Delft.
Bu, X.H., Zhang, D.M., Zhou, W.D., Jiang, Y., Jia, K., Yang, G.H., 2023. Failure process and tensile stiffness of shield tunnel with reinforced concrete inner lining under internal water pressure. Tunn. Undergr. Space Technol. 138, 105179.
Chen, Z., Yu, H., Yuan, Y., 2014. Full 3D seismic analysis of a long-distance water conveyance tunnel. Struct. Infrastruct. Eng. 10 (1), 128–140.
Chen, R.P., Chen, S., Wu, H.N., Liu, Y., Meng, F.Y., 2020. Investigation on deformation behavior and failure mechanism of a segmental ring in shield tunnels based on elaborate numerical simulation. Eng. Fail. Anal. 117, 104960.
Feng, K., He, C., Fang, Y., et al., 2013. Study on the mechanical behavior of lining structure for underwater shield tunnel of high-speed railway. Adv. Struct. Eng. 16 (8), 1381–1399.
Fibris Terre Systems GmbH, 2015. fTB 2505 Fiber-optic sensing system for distributed strain and temperature monitoring. Datasheet. www.fibristerre.de.
Forbes, B., Vlachopoulos, N., Diederichs, M.S., Hyett, A.J., Punkkinen, A., 2020. An in-situ monitoring campaign of a hard rock pillar at great depth within a Canadian mine. J. Rock Mech. Geotech. Eng. 12 (3), 427–448.
GB 50446-2017, 2017. Code for Construction and Acceptance of Shield Tunnelling Method. China Building Industry Press, Beijing (in Chinese).
GB50010-2010, 2010. Code for Design of Concrete Structures. China Building Industry Press, Beijing (in Chinese).
Guo, R., Zhang, M.Y., Xie, H.M., He, C., Fang, Y., Wang, S.M., 2019. Model test study of the mechanical characteristics of the lining structure for an urban deep drainage shield tunnel. Tunn. Undergr. Space Technol. 91, 103014.
He, H.D., Tang, X.W., Lin, S.Q., Yan, Z.R., Li, D.M., 2022. Field experiments and numerical simulations for two types of steel tube lining structures under high internal pressure Tunn. Undergr. Space Technol. 120, 104272.
Huang, H.W., Chang, J.Q., Zhang, D.M., Zhang, J., Wu, H.M., Li, G., 2022. Machine learning-based automatic control of tunneling posture of shield machine. J. Rock Mech. Geotech. Eng. 14 (4), 1153–1164.
Jin, Y., Ding, W., Yan, Z., Soga, K., Li, Z., 2017. Experimental investigation of the nonlinear behavior of segmental joints in a water-conveyance tunnel. Tunn. Undergr. Space Technol. 68, 153–166.
Kashima, Y., Kondo, N., Inoue, M., 1996. Development and application of the DPLEX shield method: results of experiments using shield and segment models and application of the method in tunnel construction. Tunn. Undergr. Space Technol. 11, 45–50.
Liu, F., Tan, C.A., Zhang, Y., Ma, T., 2021. Rockburst and microseismicity characteristics in the Qinling water conveyance tunnel of the Hanjiang-to-Weihe River diversion project. Int. J. Rock Mech. Min. 148, 104973.
Mohamad, H., Bennett, P.J., Soga, K., Mair, R.J., Bowers, K., 2010. Behaviour of an old masonry tunnel due to tunnelling–induced ground settlement. Geotechnique 60 (12), 927–938.
Molins, C., Arnau, O., 2011. Experimental and analytical study of the structural response of segmental tunnel linings based on an in situ loading test.: Part 1: test configuration and execution. Tunn. Undergr. Space Technol. 26 (6), 764–777.
Shi, B., Xu, H., Chen, B., Zhang, D., Ding, Y., Cui, H., Gao, J., 2003. A feasibility study on the application of fiber–optic distributed sensors for strain measurement in the Taiwan Strait Tunnel project. Mar. Georesour. Geotechnol. 21 (3–4), 333–343.
Soga, K., Luo, L., 2018. Distributed fiber optics sensors for civil engineering infrastructure sensing. J. Struct. Eng. 3 (1), 1–21.
Van Oorsouw, R.S., 2010. Behavior of Segment Joints in Immersed Tunnels under Seismic Loading. Delft University of Technology. MSc Thesis.
Wang, S.M., Ruan, L., Shen, X.Z., Dong, W.J., 2019. Investigation of the mechanical properties of double lining structure of shield tunnel with different joint surface. Tunn. Undergr. Space Technol. 90, 404–419.
Wang, D.Y., Zhu, H.H., Huang, J.W., Yan, Z.U., Zheng, X., Shi, B., 2023. Fiber optic sensing and performance evaluation of a water conveyance tunnel with composite linings under super-high internal pressures. J. Rock Mech. Geotech. Eng.

15 (8), 1997–2012.
Yang, C.S., Mo, H.H., Chen, J.S., 2013. Numerical study on material optimization of the composite lining of shield tunneling. Electron. J. Geotech. Eng. 18, 3813–3824.
Yang, F., Cao, S., Qin, G., 2018. Performance of the prestressed composite lining of a tunnel: case study of the Yellow River crossing tunnel. Int. J. Civ. Eng. 16, 229–241.
Yang, J.H., Zhang, X.P., Ji, P.Q., Liu, Q.S., Lu, X.J., Wei, J.P., Qi, S.H., Fang, H.G., Fang, J.N., Geng, Y.J., 2019. Analysis of disc cutter damage and consumption of TBM1 section on water conveyance tunnel at Lanzhou water source construction engineering. Tunn. Undergr. Space Technol. 85, 67–75.
Zhang, X., Broere, W., 2023a. Design of a distributed optical fiber sensor system for measuring immersed tunnel joint deformations. Tunn. Undergr. Space Technol. 131, 104770.
Zhang, X., Broere, W., 2023b. Monitoring of tidal variation and temperature change-induced movements of an immersed tunnel using distributed optical fiber sensors (DOFSs). Struct. Control Health Moni. 2419495.
Zhang, X., Broere, W., 2023c. Monitoring seasonal deformation behavior of an immersed tunnel with distributed optical fiber sensors. Measurement 219, 113268.
Zhang, L., Feng, K., Gou, C., He, C., Liang, K., Zhang, H.H., 2019. Failure tests and bearing performance of prototype segmental linings of shield tunnel under high water pressure. Tunn. Undergr. Space Technol. 92 (3), 103053.
Zhang, Z., Liu, W., Huang, X., Wang, S., 2022. Exploring the three-dimensional response of water storage and sewage tunnel based on 3D finite element modeling. Tunn. Undergr. Space Technol. 120, 104269.
Zhou, S.H., Liu, C., Li, X., Jin, H., 2017. Reverse calculation and analysis of measured internal force of deeply buried shield tunnels with large cross-section under high water pressure conditions. J. Tongji Univ. Nat. Sci. 45 (7), 970–977 (in Chinese).
Zhou, L., Shen, Y., Guan, L., Yan, Z., Sun, W., Li, Y., 2022. Full-scale experiment for segmental linings of deep-buried shield tunnels bearing high inner water pressure: comparison of mechanical behaviors of continuous- and stagger-jointed structures. Undergr. Space 8, 252–266.
Zhu, H.H., Wang, D.Y., Shi, B., Wang, X., Wei, G.Q., 2022. Performance monitoring of a curved shield tunnel during adjacent excavations using fiber optic nervous sensing system. Tunn. Undergr. Space Technol. 124, 104483.

Dr. Hong-Hu Zhu is currently Professor at School of Earth Sciences and Engineering and Dean of Institute of Earth Exploration and Sensing, Nanjing University, China. He holds a PhD in Geotechnical Engineering from the Hong Kong Polytechnic University. His research interests primarily lie in fiber optic monitoring and stability analysis of geoengineering issues, with a particular emphasis on geo-interface behaviors. His research outputs have been transformed and applied in many projects, such as landslide monitoring in the Three Gorges Reservoir area, debris flow prevention in Wenchuan earthquake zone, and structural health monitoring of the Pearl River Delta water conveyance tunnel. Over the past decade, he has co-authored 2 books, 12 patents, and over 100 journal and conference papers. In recognition of his contributions to engineering geology and geotechnics, he was awarded the 1st-class Prize of National Scientific & Technological Progress Award of China in 2018 and was granted funding from the National Science Fund for Distinguished Young Scholars in 2022. He serves as an editorial board member of *the Journal of Rock Mechanics and Geotechnical Engineering* (*JRMGE*) and five other international journals.